

Schwarzschild and Ledoux are equivalent on evolutionary timescales

EVAN H. ANDERS,^{1,2} ADAM S. JERMYN,^{3,2} DANIEL LECOANET,^{1,4,2} ADRIAN E. FRASER,^{5,2} IMOGEN G. CRESSWELL,^{6,2} AND
J. R. FUENTES⁷

¹CIERA, Northwestern University, Evanston IL 60201, USA

²Kavli Institute for Theoretical Physics, University of California, Santa Barbara, CA 93106, USA

³Center for Computational Astrophysics, Flatiron Institute, New York, NY 10010, USA

⁴Department of Engineering Sciences and Applied Mathematics, Northwestern University, Evanston IL 60208, USA

⁵University of California, Santa Cruz, Santa Cruz, California 95064, U.S.A

⁶Department Astrophysical and Planetary Sciences & LASP, University of Colorado, Boulder, CO 80309, USA

⁷Department of Physics and McGill Space Institute, McGill University, 3600 rue University, Montreal, QC H3A 2T8, Canada

(Received; Revised; Accepted; Published)

Submitted to ApJ

ABSTRACT

In one-dimensional stellar evolution models, convective boundaries are calculated using either the Schwarzschild or Ledoux criterion, but there is no consensus regarding which criterion to use. In this letter, we present a 3D hydrodynamical simulation of a convection zone whose boundary is thermally unstable but compositionally stable. Therefore, the convective boundary is Schwarzschild unstable but Ledoux stable. Over many convective overturn timescales, entrainment makes the convection zone grow. The convective boundary stops advancing after it becomes stable by the Schwarzschild criterion. This work demonstrates using 3D simulations that the Ledoux criterion *instantaneously* describes the boundary of a convection zone, but that Ledoux-stable boundaries are fragile unless they are also Schwarzschild stable. Therefore, the Schwarzschild stability criterion describes the size of a convection zone, except during short-lived evolutionary stages in which entrainment persists.

Keywords: Stellar convection zones (301), Stellar physics (1621); Stellar evolutionary models (2046)

1. INTRODUCTION

Observations tell us that we do not understand the positioning of convective boundaries in stars. For example, models and observations disagree about the sizes of convective cores (Claret & Torres 2018; Viani & Basu 2020; Pedersen et al. 2021; Johnston 2021), lithium abundances in solar-type stars (Pinsonneault 1997; Sestito & Randich 2005; Carlos et al. 2019; Dumont et al. 2021), and the sound speed at the base of the Sun’s convection zone (see Basu 2016, Sec. 7.2.1). Improperly estimating convective boundary locations can have important impacts across astrophysics such as by affecting the mass of stellar remnants (Farmer et al. 2019; Mehta et al. 2022)

and the inferred radii of exoplanets (Basu et al. 2012; Morrell 2020).

While convective boundary mixing (CBM) has many uncertainties, the most fundamental question is: what determines the location of convection zone boundaries? Some authors evaluate the *Schwarzschild criterion*, which determines where the temperature and pressure stratification within a star are stable or unstable. Others evaluate the *Ledoux criterion*, which accounts for stability or instability due to compositional stratification (e.g., the variation of helium abundance with pressure; see Salaris & Cassisi 2017, chapter 3, which reviews these criteria). Recent authors state that these criteria should be equivalent at a convective boundary according to mixing length theory (Gabriel et al. 2014; Paxton et al. 2018, 2019), but in practice these criteria are often different at convective boundaries in stellar evolution software instruments, and a variety of workarounds

have been proposed to address this (Paxton et al. 2018, 2019).

There is still disagreement regarding which stability criterion to employ (discussed in Kaiser et al. 2020, chapter 2). Multi-dimensional simulations show that convection zones with Ledoux-stable boundaries expand by entraining compositionally-stable regions (Meakin & Arnett 2007; Woodward et al. 2015; Jones et al. 2017; Cristini et al. 2019; Fuentes & Cumming 2020; Androssy et al. 2020, 2021). It is unclear from past 3D simulations whether that entrainment should stop, leading to uncertainty in how to include entrainment in 1D models (Staritsin 2013; Scott et al. 2021).

In this letter, we present a simple 3D hydrodynamical simulation that demonstrates that convection zones with Ledoux-stable but Schwarzschild-unstable boundaries entrain material until the Ledoux and Schwarzschild criteria agree on the location of the convective boundary. Therefore, in 1D stellar evolution models, when evolutionary timescales are much larger than the convective overturn timescale (such as on the main sequence, see Georgy et al. 2021), the Schwarzschild criterion describes the location of the convective boundary, and Ledoux and Schwarzschild should agree if properly implemented. We discuss these criteria in Sec. 2, display simulations in Sec. 3, and briefly discuss in Sec. 4.

2. THEORY & EXPERIMENT

Convective stability can be determined using the Schwarzschild criterion,

$$\mathcal{Y}_S \equiv \nabla_{\text{rad}} - \nabla_{\text{ad}}, \quad (1)$$

or the Ledoux criterion,

$$\mathcal{Y}_L \equiv \mathcal{Y}_S + \frac{\chi_\mu}{\chi_T} \nabla_\mu. \quad (2)$$

The temperature gradient $\nabla \equiv d \ln P / d \ln T$ (pressure P and temperature T) is ∇_{ad} for an adiabatic stratification and ∇_{rad} if the flux is entirely carried radiatively. The composition gradient $\nabla_\mu = d \ln \mu / d \ln P$ (mean molecular weight μ) is modified by $\chi_T = (d \ln P / d \ln T)_{\rho, \mu}$ and $\chi_\mu = (d \ln P / d \ln \mu)_{\rho, T}$ (density ρ).

In Eqns. 1 and 2, \mathcal{Y} is the discriminant (e.g., Paxton et al. 2018, sec. 2), which is like the superadiabaticity. Stellar structure software instruments assume that convective boundaries coincide with the root (sign change) of the discriminant. The various stability regimes which can occur in stars are described in section 3 and figure 3 of Salaris & Cassisi (2017), but note four important regimes:

1. Convection Zones (CZs): Regions with $\mathcal{Y}_S > 0$ and $\mathcal{Y}_L \geq \mathcal{Y}_S$ are convectively unstable.

2. Radiative Zones (RZs): Regions with $\mathcal{Y}_S < 0$ and $\mathcal{Y}_L \leq \mathcal{Y}_S$ are stable to convection.

3. “Semiconvection” Zones (SZs): Regions with $\mathcal{Y}_S > 0$ but $\mathcal{Y}_L < 0$ are stabilized to convection by a composition gradient despite an unstable thermal stratification. These regions can be stable RZs or linearly unstable to overstable doubly diffusive convection (ODDC, see Garaud 2018, chapter 2).

4. “Thermohaline” Zones: Regions with $\mathcal{Y}_S < 0$ and $\mathcal{Y}_L > \mathcal{Y}_S$ are thermally stable to convection despite an unstable composition gradient. These regions can be stable RZs or linearly unstable to thermohaline mixing (see Garaud 2018, chapter 3).

In this paper, we study 3D simulations of a stable SZ (#3) bounded below by a CZ (#1) and above by an RZ (#2). We examine how the boundary of the CZ evolves through entrainment. In particular, we are interested in seeing if the roots of \mathcal{Y}_S and \mathcal{Y}_L coincide after evolution.

In this work, we utilize a simplified 3D model employing the Boussinesq approximation, which assumes that the depth of the layer being studied is much smaller than the local scale height. Since we are studying thin regions near convective boundaries, this assumption is okay. The relevant physics for this problem are included (∇_{rad} varies with height, buoyancy is determined both by the composition μ and the temperature stratification T), so \mathcal{Y}_S and \mathcal{Y}_L are meaningfully defined and distinct from one another when composition gradients are present. For details on our model setup and Dedalus simulations, we refer the reader to appendices A and B.

3. RESULTS

Fig. 1 visualizes the composition field in our simulation near the initial state (left) and evolved state (right). Overplotted horizontal lines correspond to the roots of \mathcal{Y}_L (orange, Ledoux boundary) and \mathcal{Y}_S (purple, Schwarzschild boundary). Initially, the bottom third of the domain is a CZ, the middle third is an SZ, and the top third is an RZ. Convection mechanically overshoots at all times, which can be seen by the presence of convection slightly above the orange Ledoux boundary. Overshoot occurs because the Ledoux boundary corresponds to the sign change in the buoyant acceleration, not where the convective velocity is zero.

The most obvious change from the left to the right panel is that the CZ has consumed the SZ and fills the bottom two-thirds of the box. The overshooting convective motions entrained low-composition material from above the Ledoux boundary into the CZ. Convective motions mixed this fluid, and this process repeated over thousands of convective overturn times until the

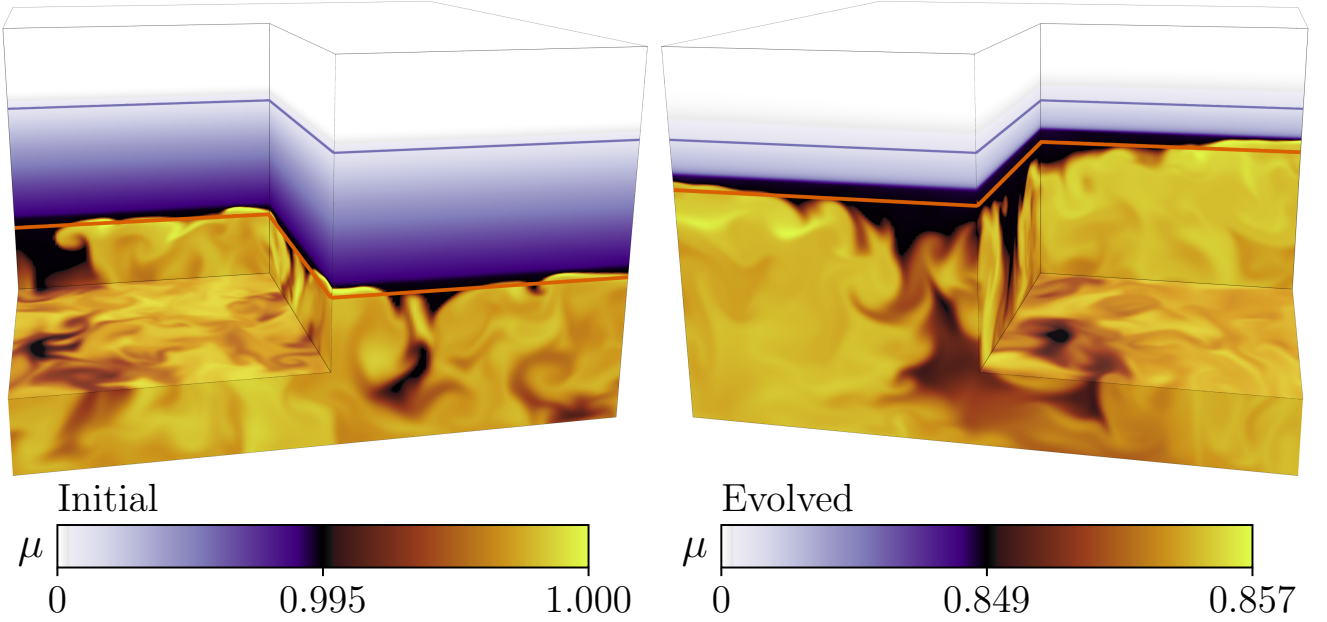


Figure 1. Volume renderings of the simulation composition field μ at early (left) and late (right) times. The change in color from white at the top of the box to dark purple at the top of the convection zone denotes a stable composition gradient. The convection zone is mostly well-mixed, so we expand the colorbar scaling there; black represents entrained low- μ fluid being mixed into the yellow high- μ convection zone. The orange and purple horizontal lines respectively denote the Ledoux and Schwarzschild boundaries. The simulation domain spans $z = [0, 3]$, but we only plot $z = [0, 2.5]$ here. *Note: this is currently evolving further.*

154 Ledoux and Schwarzschild boundaries of the CZ coincided. After becoming Schwarzschild stable, the
 155 convective boundary stopped moving. This occurs because
 156 the radiative flux renews and reinforces the radiative
 157 gradient, but there is no equivalent process for the com-
 158 position.

160 Figure 2 displays vertical simulation profiles in the
 161 initial (left) and evolved (right) states. Shown are the
 162 composition μ (top), the discriminants \mathcal{Y}_L and \mathcal{Y}_S (mid-
 163 dle), and the square Brunt-Väisälä frequency (top) as
 164 well as the square convective frequency defined as

$$f_{\text{conv}}^2 = \frac{|\mathbf{u}|^2}{\ell_{\text{conv}}^2}, \quad (3)$$

166 where \mathbf{u} is the velocity and ℓ_{conv} is the depth of the
 167 convectively unstable layer.

168 Initially, the composition is uniform in the CZ ($z < 1$)
 169 and RZ ($z > 2$), but varies linearly in the SZ ($z \in [1, 2]$).
 170 The root of \mathcal{Y}_L occurs at $z \approx 1$ while that of \mathcal{Y}_S occurs at
 171 $z \approx 2$. Furthermore, $f_{\text{conv}}^2 = 0$ in the initial, stationary
 172 state. The Brunt-Väisälä frequency N^2 is negative in a
 173 boundary layer at the base of the CZ which drives the

174 instability. N^2 is stable for $z \gtrsim 1$, and is larger in the
 175 RZ than the SZ by an order of magnitude¹

176 The evolved state is attained after convection entrains
 177 and mixes the stabilizing fluid in the SZ. We see that the
 178 composition profile (top) is constant in the CZ and over-
 179 shoot zone (denoted as a transparent hashed region), but
 180 approximates a step function at the top of the overshoot
 181 zone. The roots of the discriminants \mathcal{Y}_L and \mathcal{Y}_S coin-
 182 cide (middle). Furthermore, in the CZ, the convective
 183 frequency is roughly constant and $N^2 \lesssim 0$ (bottom). In
 184 the RZ, $f_{\text{conv}}^2 \approx 0$ and $N^2 \gg 0$. We can compute the
 185 “stiffness” of the radiative-convective interface,

$$\mathcal{S} = \frac{N^2|_{\text{RZ}}}{f_{\text{conv}}^2|_{\text{CZ}}}, \quad (4)$$

187 which is related to the oft-studied Richardson number.
 188 In our evolved simulation, we measure $\mathcal{S} \sim 10^4$. Bound-
 189 aries with a low stiffness $\mathcal{S} \lesssim 10$ easily deform in the
 190 presence of convective flows, but convective boundaries
 191 in stars often have $\mathcal{S} \gtrsim 10^6$. The number of convective
 192 overturn times required to entrain the SZ scale with \mathcal{S} ;
 193 we have chosen to use a large value of \mathcal{S} here to en-

¹ We ran simulations where N^2 was identical in the RZ and SZ and saw similar behavior. We make N^2 large in the RZ to reduce overshoot and wave mixing in the evolved state.

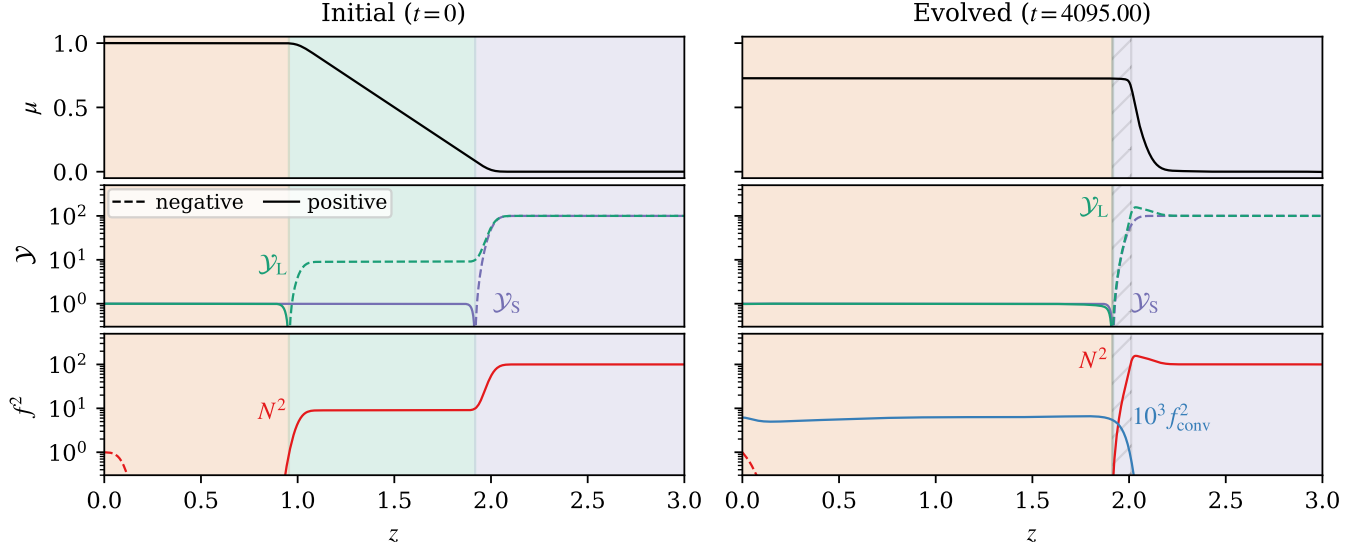


Figure 2. Horizontally-averaged profiles are shown for the composition (top), the discriminants γ_S and γ_L (middle, Eqs. 1 & 2), and the Brunt-Väisälä frequency $N^2 = -\gamma_L$ and the square convective frequency f_{conv}^2 (bottom, Eqn. 3). Positive and negative values are respectively solid and dashed lines. We show the initial (left) and evolved (right, time-averaged over 100 convective overturn times) states. Note that there are no motions in the initial state, so $f_{\text{conv}}^2 = 0$ and does not appear. The background color is orange in CZs, green in SZs, and purple in RZs per Section 2. The lightly hashed background region in the evolved RZ is the mechanical overshoot zone. **Note: this data is taken from a less turbulent run than fig 1; it'll be updated when the fig 1 run finishes.**

sure our simulations are in the right regime to study entrainment at a stellar convective boundary. We briefly note that the entrainment timescale for the SZ scales like $\mathcal{S}^\alpha \tau_{\text{dyn}}$, where α is an $\mathcal{O}(1)$ positive exponent and τ_{dyn} is the dynamical timescale. Since the relevant timescale of evolution on the main sequence is the nuclear time τ_{nuc} , and since $\tau_{\text{nuc}}/\tau_{\text{dyn}} \gg \mathcal{S}^\alpha$ even for $\mathcal{S} \sim 10^6$, we expect CZs to entrain SZs during a single stellar evolution time step.

Finally, Figure 3 displays a Kippenhahn-like diagram of the simulation's height vs. time to show evolutionary trends. The roots of γ_L and γ_S are respectively shown as orange (Ledoux boundary) and purple (Schwarzschild boundary) lines. The CZ is colored orange and sits below the Ledoux boundary, the RZ is colored purple and sits above the Schwarzschild boundary, and the SZ is colored green and is between these boundaries. Convection motions overshoot above the Ledoux boundary. The height where the horizontally-averaged kinetic energy falls below 10% of its bulk-CZ value is marked with a black line, and the hashed region below it is the overshoot zone. We note that the black line and overshoot zone roughly correspond with the maximum of $\partial\mu/\partial z$ (Fig. 2, upper right), so this describes overshoot well. Importantly, note that the Schwarzschild and Ledoux boundaries start at different heights, but 3D convective mixing causes them to converge on dynamical timescales.

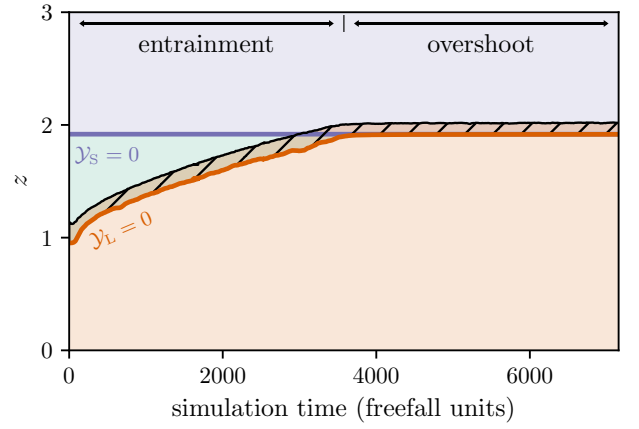


Figure 3. A Kippenhahn-like diagram of the simulation evolution. The y -axis is simulation height and the x -axis is simulation time. The orange line denotes the Ledoux boundary ($\gamma_L = 0$); the CZ is below this and is colored orange. The purple line denotes the Schwarzschild boundary ($\gamma_S = 0$); the RZ is above this and is colored purple. The semiconvective region between these boundaries is colored green. The overshoot zone is hashed, and the black line denotes the top of this region. The simulation has an “entrainment phase” while the CZ expands, and a pure “overshoot phase” where the convective boundary does not advance. **Note: this data is taken from a less turbulent run than fig 1; it'll be updated when the fig 1 run finishes.**

4. CONCLUSIONS & DISCUSSION

In this letter, we presented a 3D simulation of a convection zone and its boundary. The convective boundary was initially compositionally stable but weakly thermally unstable (Ledoux stable but Schwarzschild unstable). Entrainment caused the convective boundary to advance until the boundary was stable by both the Schwarzschild and Ledoux criteria.

This simulation demonstrates that the Ledoux criterion *instantaneously* describes the location of a convective boundary. However, when the dynamical convective overturn timescale is short compared to the evolutionary timescale $t_{\text{evol}} \gg \mathcal{S}^\alpha t_{\text{dyn}}$ (see Sec. 3), the statistically-stationary location of the convective boundary will coincide with the Schwarzschild boundary. These 3D dynamics support the claim that “logically consistent” implementations of mixing length theory (Gabriel et al. 2014; Paxton et al. 2018, 2019) should have convective boundaries which are Schwarzschild-stable. Modern algorithms like the MESA software instrument’s “convective pre-mixing” (CPM, Paxton et al. 2019) should agree with our results. The results of 1D stellar evolution calculations should not depend on the choice of stability criterion used when $t_{\text{evol}} \gg \mathcal{S}^\alpha t_{\text{dyn}}$.

We note briefly that many SZs (the middle layer of our simulations) in stars are unstable to overstably doubly-diffusive convection (ODDC). ODDC mixes composition gradients even more rapidly than the entrainment studied here, and has been studied extensively in local simulations (Mirouh et al. 2012; Wood et al. 2013; Xie et al. 2017); see the review of Garaud (2018). Moore & Garaud (2016) apply ODDC to the regions outside core convection zones in main sequence stars, and their results suggest that ODDC formulations should be widely included in stellar models.

For stages in stellar evolution where $\mathcal{S}^\alpha t_{\text{dyn}} \sim t_{\text{evol}}$, implementations of time-dependent convection (TDC, Kuhfuss 1986) should be employed to properly capture convective dynamics and the advancement of convective

boundaries. The advancement of convective boundaries by e.g., entrainment in TDC implementations should be informed by time-dependent theories and simulations (e.g., Turner 1968; Fuentes & Cumming 2020).

The purpose of this study was to understand how the Ledoux boundary location evolves over time, and whether it coincides with the Schwarzschild boundary at late times. A detailed examination of convective overshoot is beyond the scope of this work (but see e.g., Korre et al. 2019). We furthermore constructed the simulations in this work to have negligible convective penetration per Anders et al. (2021). Finally, in stars, ∇_{rad} and the Schwarzschild boundary location depend upon μ , but we made the assumption that the radiative conductivity and ∇_{rad} do not depend on μ for simplicity. The nonlinear feedback between these effects should be studied in future work, but we do not expect that the fundamental takeaways of this work should change.

In summary, we find that the Ledoux criterion provides the instantaneous location of the convective boundary, and the Schwarzschild criterion provides the location of the convective boundary in a statistically stationary state; in this final state, the Ledoux and Schwarzschild criteria agree.

We thank Meridith Joyce, Anne Thoul, Dominic Bowman, Jared Goldberg, Tim Cunningham, Falk Herwig, Kyle Augustson, (OTHERS?) for useful discussions which helped improve our understanding. EHA is funded as a CIERA Postdoctoral fellow and would like to thank CIERA and Northwestern University. This research was supported in part by the National Science Foundation under Grant No. PHY-1748958, and we acknowledge the hospitality of KITP during the Probes of Transport in Stars Program. Computations were conducted with support from the NASA High End Computing (HEC) Program through the NASA Advanced Supercomputing (NAS) Division at Ames Research Center on Pleiades with allocation GID s2276. The Flatiron Institute is supported by the Simons Foundation.

APPENDIX

A. MODEL & INITIAL CONDITIONS

In this work we study the simplest possible system: incompressible, Boussinesq convection with a composition

field. These equations are

$$\nabla \cdot \mathbf{u} = 0 \quad (\text{A1})$$

$$\partial_t \mathbf{u} + \mathbf{u} \cdot \nabla \mathbf{u} + \nabla \varpi = \left(T - \frac{\mu}{R_0} \right) \hat{z} + \frac{\text{Pr}}{\text{Pe}} \nabla^2 \mathbf{u}, \quad (\text{A2})$$

$$\partial_t T + \mathbf{u} \cdot (\nabla T - \hat{z} \partial_z T_{\text{ad}}) + \nabla \cdot [-\kappa_{T,0} \nabla \bar{T}] = \frac{1}{\text{Pe}} \nabla^2 T', \quad (\text{A3})$$

$$\partial_t \mu + \mathbf{u} \cdot \nabla \mu = -\frac{\tau_0}{\text{Pe}} \nabla^2 \bar{\mu} + \frac{\tau}{\text{Pe}} \nabla^2 \mu'. \quad (\text{A4})$$

Here, \mathbf{u} is velocity, T is temperature, and μ is concentration. Bars (e.g., \bar{T}) represent the horizontally-averaged component of a field and primes (e.g., T') denote all fluctuations around that background. The adiabatic temperature gradient is $\partial_z T_{\text{ad}}$ and the nondimensional control parameters are

$$\begin{aligned} \text{Pe} &= \frac{u_{\text{ff}} \ell_{\text{conv}}}{\kappa_T}, & R_0 &= \frac{|\alpha| \Delta T}{|\beta| \Delta \mu}, \\ \text{Pr} &= \frac{\nu}{\kappa_T}, & \tau &= \frac{\kappa_\mu}{\kappa_T}, \end{aligned} \quad (\text{A5})$$

where the nondimensional freefall velocity is $u_{\text{ff}} = \sqrt{|\alpha| g \ell_{\text{conv}} \Delta T}$ (with gravitational acceleration g), ℓ_{conv} is the initial depth of the convection zone, $\Delta \mu$ is the composition change across the Ledoux stable region, $\Delta T = \ell_{\text{conv}} (\partial_z T_{\text{rad}} - \partial_z T_{\text{ad}})$ is the superadiabatic temperature scale of the convection zone, α and β are the coefficients of expansion for T and μ , ν is the viscosity, κ_T is the thermal diffusivity, and κ_μ is the compositional diffusivity. Eqns. A1-A4 are identical to Eqns. 2-5 in [Garaud \(2018\)](#), except we modify the diffusion coefficients acting on \bar{T} ($\kappa_{T,0}$) and $\bar{\mu}$ (τ_0). By doing this, the radiative temperature gradient $\partial_z T_{\text{rad}} = -\text{Flux}/\kappa_{T,0}$ can change with height, and we reduce diffusion on $\bar{\mu}$ to ensure its evolution is due to advection.

We define the Ledoux and Schwarzschild discriminants

$$\mathcal{Y}_S = \left(\frac{\partial T}{\partial z} \right)_{\text{rad}} - \left(\frac{\partial T}{\partial z} \right)_{\text{ad}}, \quad \mathcal{Y}_L = \mathcal{Y}_S - R_0^{-1} \frac{\partial \mu}{\partial z}, \quad (\text{A6})$$

and in this nondimensional system the Brunt-Väisälä frequency is the negative of the Ledoux discriminant $N^2 = -\mathcal{Y}_L$.

In this work, we study a three-layer model in $z = [0, 3]$,

$$\left(\frac{\partial T}{\partial z} \right)_{\text{rad}} = \left(\frac{\partial T}{\partial z} \right)_{\text{ad}} + \begin{cases} -1 & z \leq 2 \\ 10R_0^{-1} & z > 2 \end{cases}, \quad (\text{A7})$$

$$\frac{\partial \mu_0}{\partial z} = \begin{cases} 0 & z \leq 1 \\ -1 & 1 < z \leq 2 \\ 0 & 2 < z \end{cases}, \quad (\text{A8})$$

We set $\mu = 1$ at $z = 0$ and $T = 1$ at $z = 3$. The initial temperature profile has $\partial_z T_0 = \partial_z T_{\text{rad}}$ everywhere except between $z = [0.1, 1]$ where $\partial_z T_0 = \partial_z T_{\text{ad}}$. We set $(\partial T / \partial z)_{\text{ad}} = -1 - 10R_0^{-1}$.

B. SIMULATION DETAILS & DATA AVAILABILITY

We time-evolve equations A1-A4 using the Dedalus pseudospectral solver ([Burns et al. 2020](#), git commit 1339061) using timestepper SBDF2 ([Wang & Ruuth 2008](#)) and safety factor 0.3. All variables are spectral expansions of Chebyshev coefficients in the vertical (z) direction ($n_z = 512$ between $z = [0, 2.25]$ plus $n_z = 64$ between $z = [2.25, 3]$) and as $(n_x, n_y) = (192, 192)$ Fourier coefficients in the horizontally periodic (x, y) directions. Our domain spans $x \in [0, L_x]$, $y \in [0, L_y]$, and $z \in [0, L_z]$ with $L_x = L_y = 4$ and $L_z = 3$. To avoid aliasing errors, we use the 3/2-dealiasing rule in all directions. To start our simulations, we add random noise temperature perturbations with a magnitude of 10^{-6} to the initial temperature profile.

Spectral methods with finite coefficient expansions cannot capture true discontinuities. To approximate discontinuous functions such as Eqns. A7 & A8, we define a smooth Heaviside step function centered at $z = z_0$,

$$H(z; z_0, d_w) = \frac{1}{2} \left(1 + \text{erf} \left[\frac{z - z_0}{d_w} \right] \right). \quad (\text{B9})$$

where erf is the error function and we set $d_w = 0.05$. The simulation in this work uses $\mathcal{P} = 3.2 \times 10^3$, $R_0^{-1} = 10$, $\text{Pr} = \tau = 0.5$, $\tau_0 = 1.5 \times 10^{-3}$, and $\kappa_{T,0} = \mathcal{P}^{-1} [(\partial T / \partial z)_{\text{rad}}|_{z=0}] / (\partial T / \partial z)_{\text{rad}}$.

We produce figures 2 and 3 using matplotlib ([Hunter 2007](#); [Caswell et al. 2021](#)). We produce figure 1 using plotly ([Inc. 2015](#)) and matplotlib. All of the Python scripts used to run the simulations in this paper and to create the figures in this paper are publicly available in a git repository (https://github.com/evanhandlers/schwarzschild_or_ledoux) and in a Zenodo repository (?).

REFERENCES

- Anders, E. H., Jermyn, A. S., Lecoanet, D., & Brown, B. P. 2021, arXiv e-prints, arXiv:2110.11356.
<https://arxiv.org/abs/2110.11356>
- Andrassy, R., Herwig, F., Woodward, P., & Ritter, C. 2020, MNRAS, 491, 972, doi: [10.1093/mnras/stz2952](https://doi.org/10.1093/mnras/stz2952)
- Andrassy, R., Higl, J., Mao, H., et al. 2021, arXiv e-prints, arXiv:2111.01165. <https://arxiv.org/abs/2111.01165>
- Basu, S. 2016, Living Reviews in Solar Physics, 13, 2, doi: [10.1007/s41116-016-0003-4](https://doi.org/10.1007/s41116-016-0003-4)
- Basu, S., Verner, G. A., Chaplin, W. J., & Elsworth, Y. 2012, ApJ, 746, 76, doi: [10.1088/0004-637X/746/1/76](https://doi.org/10.1088/0004-637X/746/1/76)
- Burns, K. J., Vasil, G. M., Oishi, J. S., Lecoanet, D., & Brown, B. P. 2020, Physical Review Research, 2, 023068, doi: [10.1103/PhysRevResearch.2.023068](https://doi.org/10.1103/PhysRevResearch.2.023068)
- Carlos, M., Meléndez, J., Spina, L., et al. 2019, MNRAS, 485, 4052, doi: [10.1093/mnras/stz681](https://doi.org/10.1093/mnras/stz681)
- Caswell, T. A., Droettboom, M., Lee, A., et al. 2021, matplotlib/matplotlib: REL: v3.3.4, v3.3.4, Zenodo, doi: [10.5281/zenodo.4475376](https://doi.org/10.5281/zenodo.4475376)
- Claret, A., & Torres, G. 2018, ApJ, 859, 100, doi: [10.3847/1538-4357/aabd35](https://doi.org/10.3847/1538-4357/aabd35)
- Cristini, A., Hirschi, R., Meakin, C., et al. 2019, MNRAS, 484, 4645, doi: [10.1093/mnras/stz312](https://doi.org/10.1093/mnras/stz312)
- Dumont, T., Palacios, A., Charbonnel, C., et al. 2021, A&A, 646, A48, doi: [10.1051/0004-6361/202039515](https://doi.org/10.1051/0004-6361/202039515)
- Farmer, R., Renzo, M., de Mink, S. E., Marchant, P., & Justham, S. 2019, ApJ, 887, 53, doi: [10.3847/1538-4357/ab518b](https://doi.org/10.3847/1538-4357/ab518b)
- Fuentes, J. R., & Cumming, A. 2020, Physical Review Fluids, 5, 124501, doi: [10.1103/PhysRevFluids.5.124501](https://doi.org/10.1103/PhysRevFluids.5.124501)
- Gabriel, M., Noels, A., Montalbán, J., & Miglio, A. 2014, A&A, 569, A63, doi: [10.1051/0004-6361/201423442](https://doi.org/10.1051/0004-6361/201423442)
- Garaud, P. 2018, Annual Review of Fluid Mechanics, 50, 275, doi: [10.1146/annurev-fluid-122316-045234](https://doi.org/10.1146/annurev-fluid-122316-045234)
- Georgy, C., Saio, H., & Meynet, G. 2021, A&A, 650, A128, doi: [10.1051/0004-6361/202040105](https://doi.org/10.1051/0004-6361/202040105)
- Hunter, J. D. 2007, Computing in Science and Engineering, 9, 90, doi: [10.1109/MCSE.2007.55](https://doi.org/10.1109/MCSE.2007.55)
- Inc., P. T. 2015, Collaborative data science, Montreal, QC: Plotly Technologies Inc. <https://plot.ly>
- Johnston, C. 2021, A&A, 655, A29, doi: [10.1051/0004-6361/202141080](https://doi.org/10.1051/0004-6361/202141080)
- Jones, S., Andrassy, R., Sandalski, S., et al. 2017, MNRAS, 465, 2991, doi: [10.1093/mnras/stw2783](https://doi.org/10.1093/mnras/stw2783)
- Kaiser, E. A., Hirschi, R., Arnett, W. D., et al. 2020, MNRAS, 496, 1967, doi: [10.1093/mnras/staa1595](https://doi.org/10.1093/mnras/staa1595)
- Korre, L., Garaud, P., & Brummell, N. H. 2019, MNRAS, 484, 1220, doi: [10.1093/mnras/stz047](https://doi.org/10.1093/mnras/stz047)
- Kuhfuss, R. 1986, A&A, 160, 116
- Meakin, C. A., & Arnett, D. 2007, ApJ, 667, 448, doi: [10.1086/520318](https://doi.org/10.1086/520318)
- Mehta, A. K., Buonanno, A., Gair, J., et al. 2022, ApJ, 924, 39, doi: [10.3847/1538-4357/ac3130](https://doi.org/10.3847/1538-4357/ac3130)
- Mirouh, G. M., Garaud, P., Stellmach, S., Traxler, A. L., & Wood, T. S. 2012, ApJ, 750, 61, doi: [10.1088/0004-637X/750/1/61](https://doi.org/10.1088/0004-637X/750/1/61)
- Moore, K., & Garaud, P. 2016, ApJ, 817, 54, doi: [10.3847/0004-637X/817/1/54](https://doi.org/10.3847/0004-637X/817/1/54)
- Morrell, S. A. F. 2020, PhD thesis, University of Exeter
- Paxton, B., Schwab, J., Bauer, E. B., et al. 2018, ApJS, 234, 34, doi: [10.3847/1538-4365/aaa5a8](https://doi.org/10.3847/1538-4365/aaa5a8)
- Paxton, B., Smolec, R., Schwab, J., et al. 2019, ApJS, 243, 10, doi: [10.3847/1538-4365/ab2241](https://doi.org/10.3847/1538-4365/ab2241)
- Pedersen, M. G., Aerts, C., Pápics, P. I., et al. 2021, arXiv e-prints, arXiv:2105.04533. <https://arxiv.org/abs/2105.04533>
- Pinsonneault, M. 1997, ARA&A, 35, 557, doi: [10.1146/annurev.astro.35.1.557](https://doi.org/10.1146/annurev.astro.35.1.557)
- Salaris, M., & Cassisi, S. 2017, Royal Society Open Science, 4, 170192, doi: [10.1098/rsos.170192](https://doi.org/10.1098/rsos.170192)
- Scott, L. J. A., Hirschi, R., Georgy, C., et al. 2021, MNRAS, 503, 4208, doi: [10.1093/mnras/stab752](https://doi.org/10.1093/mnras/stab752)
- Sestito, P., & Randich, S. 2005, A&A, 442, 615, doi: [10.1051/0004-6361:20053482](https://doi.org/10.1051/0004-6361:20053482)
- Staritsin, E. I. 2013, Astronomy Reports, 57, 380, doi: [10.1134/S1063772913050089](https://doi.org/10.1134/S1063772913050089)
- Turner, J. S. 1968, Journal of Fluid Mechanics, 33, 183, doi: [10.1017/S00222112068002442](https://doi.org/10.1017/S00222112068002442)
- Viani, L. S., & Basu, S. 2020, ApJ, 904, 22, doi: [10.3847/1538-4357/abba17](https://doi.org/10.3847/1538-4357/abba17)
- Wang, D., & Ruuth, S. J. 2008, Journal of Computational Mathematics, 26, 838. <http://www.jstor.org/stable/43693484>
- Wood, T. S., Garaud, P., & Stellmach, S. 2013, ApJ, 768, 157, doi: [10.1088/0004-637X/768/2/157](https://doi.org/10.1088/0004-637X/768/2/157)
- Woodward, P. R., Herwig, F., & Lin, P.-H. 2015, ApJ, 798, 49, doi: [10.1088/0004-637X/798/1/49](https://doi.org/10.1088/0004-637X/798/1/49)
- Xie, J.-H., Miquel, B., Julien, K., & Knobloch, E. 2017, Fluids, 2, doi: [10.3390/fluids2010006](https://doi.org/10.3390/fluids2010006)